ACS OMEGA

http://pubs.acs.org/journal/acsodf

Article

From MOF-199 Microrods to CuO Nanoparticles for Room-Temperature Desulfurization: Regeneration and Repurposing Spent Adsorbents as Sustainable Approaches

Nishesh Kumar Gupta, Jiyeol Bae,* and Kwang Soo Kim

Cite This: *ACS Omega* 2021, 6, 25631−25641

Read Online

ACCESS | Metrics & More | Article Recommendations | Supporting Information

ABSTRACT: MOF-199 is one of the well-studied metal−organic frameworks (MOFs) for the capture of small gas molecules. In this study, we have investigated the thermal transformation of MOF-199 microrods to CuO nanoparticles by various microscopic and spectroscopic techniques. The growth of oxide was initiated by the formation of ∼2.5 nm particles at 200 °C, which ended up as CuO nanoparticles of ∼100−250 nm size at 550 °C. An intermediate presence of Cu_2O along with CuO was recorded at 280 °C. The MOF and calcined products were tested for the room-temperature desulfurization process. MOF-199 showed the maximum adsorption capacity for H_2S gas (77.1 mg g^{-1}) among all adsorbents studied. Also, MOF-199 showed a better regeneration efficiency than the derived oxide. For a sustainable process, the exhausted adsorbents were used for the photocatalytic degradation of methylene blue. The exhausted materials showed better degradation efficiencies than the fresh materials. This study reports new sustainable approaches for MOF-199 application in air and water decontamination.

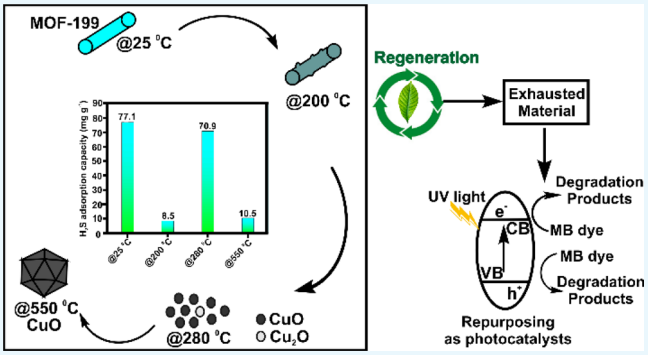

INTRODUCTION

Metal−organic frameworks (MOFs) are a unique class of inorganic−organic hybrids known for their exceptionally high surface area and porosity. These crystalline hybrid materials have found wider applications in gas separation, capture, storage, and delivery, which are associated with the flexibility and tunability of the MOF's structure driven by organic linkers.[1−4] Apart from their direct applications in energy and the environment,[5−7] MOFs serve as templates for a range of carbonaceous and noncarbonaceous materials through pyrolysis/calcination processes.[8,9] These MOF-derived materials are of great importance in the development of highly porous and morphologically preserved materials for catalysis, gas adsorption, and sensing.[10−13]

MOF-199 (also known as HKUST-1, Cu-BTC, and Basolite C300) is a copper-based microporous metal−organic framework (MOF) composed of dimeric Cu units bridged by benzene-1,3,5-tricarboxylate (BTC) linkers as a paddlewheel structure. MOF-199 is one of the most studied MOFs for gas separation, storage, and capture.[14−16] Each Cu center has a coordinated water molecule in the axial position, which creates potential binding sites for gas molecules after removal. The strong interaction of sulfide with Cu makes these uncoordinated Cu units ideal binding sites for H_2S capture.[17] For this reason, numerous reports on the use of MOF-199 for H_2S removal are available in the literature.[18−21] MOF-199 also served as the template for porous oxide-carbon and oxide composites.[22−24] In this study, we have studied the conversion of MOF-199 microrods to CuO nanoparticles as a function of temperature using various microscopic and spectroscopic techniques. The structure−property relationship among MOF-199 and calcined products was studied by considering the adsorptive removal of H_2S gas in ambient conditions.

In the literature, H_2S adsorption/oxidation over MOF-199 has been reported on numerous occasions with no significant contributions toward the regeneration of spent MOF-199.[18−21] We reported the first regeneration process based on the photoactivation of spent MOFs under UV irradiation.[21] The MOF-199 structure collapses after H_2S interaction and yields covellite (CuS) as the final product.[25] However, in our previous studies, we confirmed covellite in $Cu(BDC)_{0.5}(BDC\text{-}NH_2)_{0.5}$[26] and not in MOF-199 after H_2S exposure.[21] In this study, we have opted for a low-temperature thermal regeneration method for activating spent MOF-199 and CuO/Cu_2O.

Received: July 13, 2021
Published: September 23, 2021

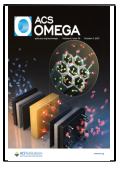

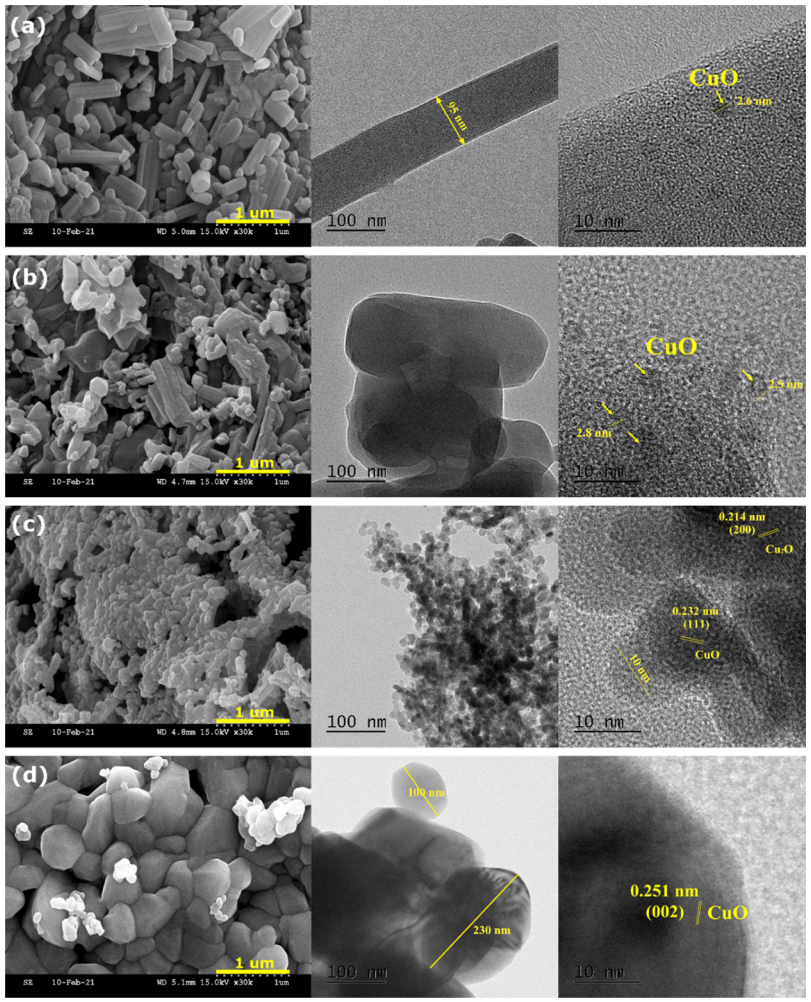

Figure 1. SEM and TEM micrographs of (a) MOF-199, (b) MOF-199-A, (c) CuO-280, and (d) CuO-550.

The concept of recycling is old, but the repurposing of exhausted materials is relatively new. After some adsorption−regeneration cycles, the adsorbent loses its capacity and is discarded as it is not feasible to regenerate on an economic front. These exhausted adsorbents should be repurposed for secondary applications so that the overall process is environmentally benign. He et al. repurposed the spent Cr-loaded silica adsorbent as an efficient catalyst for methyl mercaptan abatement and propane dehydrogenation.[27] Umejuru and coworkers repurposed the spent Cd-loaded coal fly ash/carbon composite for photocatalytic degradation of the methylene blue (MB) dye.[28] This green practice has been included in the present work, where exhausted adsorbents were studied for the improved photocatalytic degradation of the MB dye.

RESULTS AND DISCUSSION

Characterization of Adsorbents. The SEM and TEM micrographs of MOF-199 and calcination products are shown in Figure 1 and Figure S2. MOF-199 crystallized as microrods of ∼95 nm width. Since the MOF was exposed to a high-energy electron beam during the TEM analysis, CuO nanoparticles (2.6 nm size) were found deposited on the microrod surface (Figure 1a).[29] After heating at 200 °C (MOF-199-A), the microrod feature deteriorated with the increased density of CuO nanoparticles (2.5−2.8 nm) (Figure 1b). At 280 °C (CuO-280), CuO and Cu_2O nanoparticles of 10 nm size were observed. These nanoparticles were confirmed by mapping their fringe width where nanoparticles with the fringe widths of 0.214 (200) and 0.232 nm (111) were identified as Cu_2O and CuO, respectively (Figure 1c).[30] At 550 °C (CuO-550), CuO nanoparticles of 100−250 nm size formed with the absence of Cu_2O (Figure 1d). The CuO nanoparticle size increased with the increasing calcination temperature. A similar observation has been reported for the formation of Cu/Cu_2O from the pyrolysis of MOF-199 in a N_2 atmosphere.[31] The microscopic analyses confirmed the transformation of MOF-199 microrods to CuO nanoparticles with the presence of Cu_2O nanoparticles in the transition process. The nanoparticle formation over MOF microrods is delocalized in the temperature range of 70−200 °C. These nanoparticles (2.5−2.8 nm) serve as the seed for the formation of ∼10 nm sized nanoparticles at 280 °C, which further grow to large sized nanoparticles (100−250 nm) at 550 °C.

The TEM-EDAX analysis and elemental mapping are shown in Figures S3 and S4, respectively. The presence of Cu, O, C, and N was confirmed in MOF-199 and calcined products. The N peak was due to the presence of nitrate ions in the MOF (from the Cu salt). The C peak in CuO-280 was due to the traces of residual carbon, which remained in the sample due to low calcination temperature (Figure S3c). The C peak in CuO-550 was due to the carbonaceous layer deposited on the oxide surface as a result of electron bombardment. This beam-

https://doi.org/10.1021/acsomega.1c03712
ACS Omega 2021, 6, 25631−25641

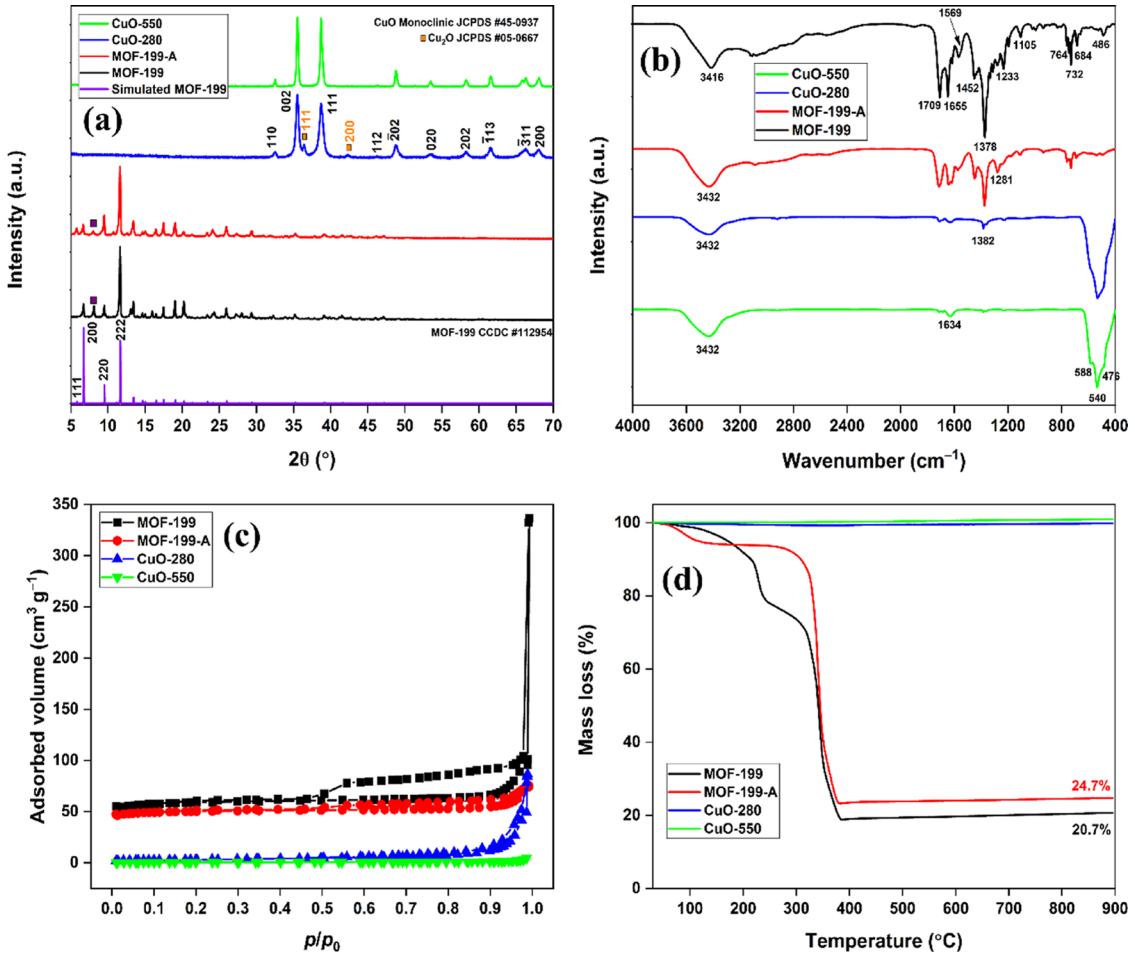

Figure 2. (a) PXRD patterns, (b) FTIR spectra, (c) N_2 adsorption−desorption isotherms, and (d) TGA profiles in a N_2/O_2 atmosphere.

induced contamination is linked to the hydrocarbons present in the TEM chamber (Figure S3d).[32] The MOF transformation to CuO was traced well with the decreasing C and increasing Cu content as a function of calcination temperature (Table S1).

The PXRD patterns of MOF-199 and calcined products are shown in Figure 2a. The diffraction pattern of synthesized MOF-199 matched well with the simulated pattern.[33] The I_{200}/I_{220} ratio for the synthesized MOF was significantly low compared to the simulated PXRD pattern. The low ratio was due to the presence of water molecules bound to the copper coordination sites.[34] The MOF-199-A pattern has diffraction peaks with diminished intensity. The decreased intensity of peaks was linked to a partial loss of MOF crystallinity at 200 °C, which was also observed in the SEM images. The (111) reflection peak, which was missing in the synthesized MOF, appeared in MOF-199-A. This peak was observed in the simulated PXRD pattern of the dehydrated MOF (Cu_3BTC_2) as well. Thus, we assumed that the loss of Cu-bound water was responsible for the appearance of the (111) reflection. Though we traced CuO nanoparticles from TEM analysis, the diffraction peaks for CuO were untraceable in the PXRD pattern of MOF-199-A, probably due to low particle density, which was below the detection limit. The PXRD pattern of CuO-280 has broad peaks for monoclinic CuO nanoparticles (JCPDS no. 45-0937)[35] with a minor presence of Cu_2O (JCPDS no. 05-0667).[36] At this temperature, the MOF was transformed to Cu_2O−CuO nanoparticles. The PXRD pattern of CuO-550 has peaks for CuO with the absence of Cu_2O, which suggested the complete oxidation of MOF-199 microrods to CuO nanoparticles. The sharpening of CuO diffraction peaks was due to the increase in the particle size,[37] which was also observed in the HRTEM images.

The FTIR spectra of MOF-199 and calcined products are shown in Figure 2b. The broad, intense band at 3416 cm^{-1} was assigned to the ν_s(OH) modes of adsorbed water molecules. The bands at 1452, 1105, and 764 cm^{-1} were for the tangential CC stretching, HCC bending, and HCC wagging, respectively, of aromatic rings. The band at 486 cm^{-1} was attributed to the Cu−O (carboxylate) stretching. The doublet at 1709 and 1655 cm^{-1} was assigned to the ν_{as}(COO) and ν_s(COO) modes of carboxylate groups located in the large pores of the framework. The most intense band at 1378 cm^{-1} was attributed to the ν_s(COO) modes placed in the smaller pores.[38] For MOF-199-A, the observed H_2O band was due to the strong affinity of the MOF for atmospheric moisture, which occurred during the sample preparation process. The intensity of all major bands decreased at 200 °C, a strong indication of compromised MOF-199 stability even at low temperatures. The intensity ratio of ν_s(COO) in the larger pores to the smaller pores was 0.64 in MOF-199. This ratio was slightly higher (~0.71) in MOF-199-A. From this, it could be safely assumed that the deterioration of Cu−O(carboxylate) bonds was more probable in the larger pores (Figure S5). For CuO-280, intense bands in 661−400 cm^{-1} were due to the Cu−O stretching vibrations of Cu_2O−CuO. At 280 °C, most of the MOF microrods were

https://doi.org/10.1021/acsomega.1c03712
ACS Omega 2021, 6, 25631−25641

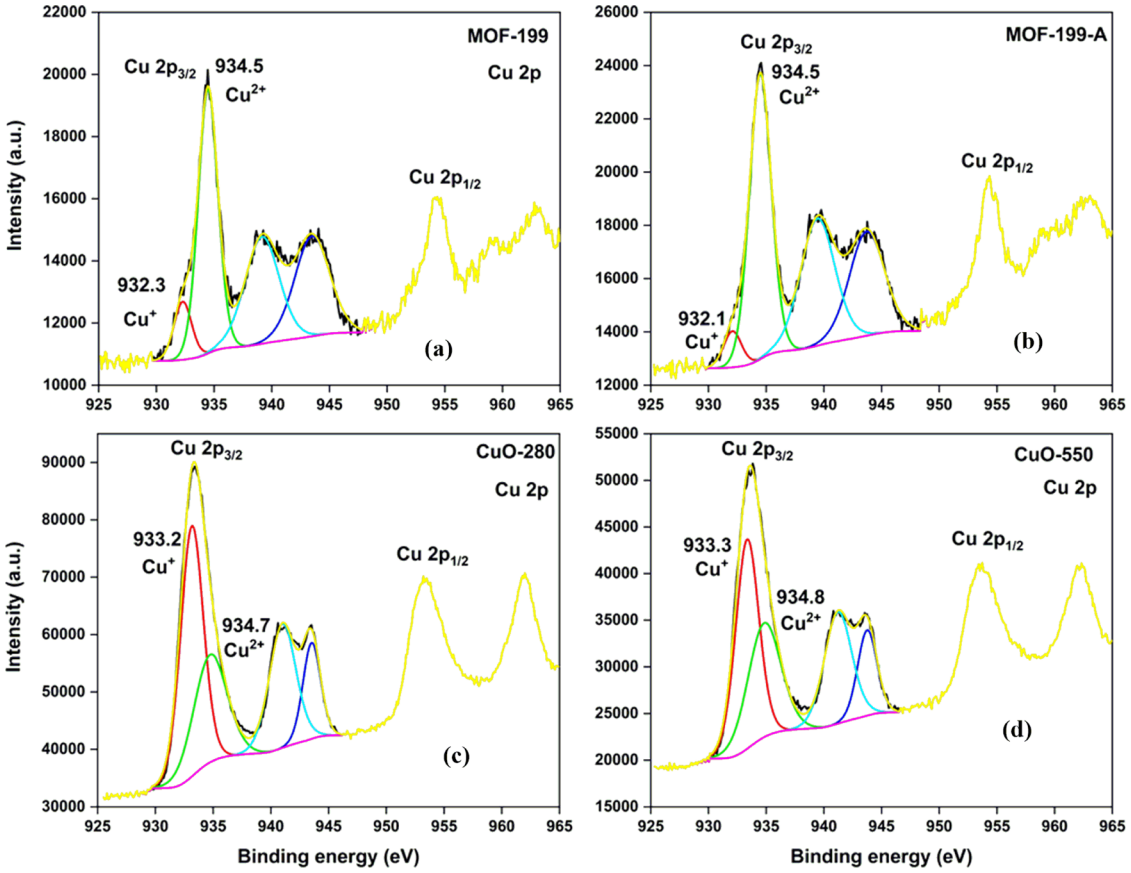

Figure 3. HRXPS Cu 2p spectra of (a) MOF-199, (b) MOF-199-A, (c) CuO-280, and (d) CuO-550.

converted to oxides with a minor presence of carboxylate bands. In CuO-550, carboxylate bands were absent. Moreover, the disappearance of Cu_2O nanoparticles shrunk the Cu−O band range to 645−400 cm^{-1} as the $\nu_s(Cu^I-O)$ modes (~630 cm^{-1}) are observed at a higher wavenumber compared to the $\nu_s(Cu^{II}-O)$ modes (~500 cm^{-1}).[23]

The N_2 adsorption−desorption isotherms are shown in Figure 2c, and the corresponding textural data are listed in Table S2. MOF-199 microrods exhibited a typical type IV isotherm.[29] The BET surface area (S_{BET}) of 231.94 m^2 g^{-1} was significantly low compared to the reported values in the literature.[39] The low surface area was due to the formation of large sized microparticles.[21] The pore diameter (D_p) of 9.0 nm suggested synthesized MOF-199 as a mesoporous material. The surface area and pore properties of MOF-199 decreased after heating at 200 °C. The drastic decreases in the pore volume (V_p) and D_p were linked to the collapsing of larger sized pores after heating, which were predicted by FTIR as well. CuO-280 has a surface area of 11.19 m^2 g^{-1} with a pore diameter of 47.9 nm. The surface area and porosity decreased at 550 °C due to increased particle size.[40]

The TGA profiles of MOF-199 and calcined products are shown in Figure 2d. The MOF-199 has three weight loss regions. The first region in the 30−110 °C range was due to the evaporation of physically adsorbed water molecules (~1.5 wt %). The second region (110−260 °C) has a weight loss of 21.5% due to the removal of chemically bonded water molecules and physically adsorbed DMF molecules. The third region (260−380 °C) was marked by a weight loss of 58.1% due to the destruction of the MOF structure and the loss of organic linkers.[41] The slight increase in weight (~1.8%) in the 380−900 °C region was due to the oxidation of Cu_2O to CuO.[42] For MOF-199-A, a 5% weight loss was observed in the first region. The affinity for moisture was thought to increase in MOF-199-A. For this reason, physically adsorbed water molecules were traced in the sample. An insignificant weight loss was observed in the second region due to the pre-removal of water molecules and DMF. The removal of axial ligands (DMF/water) and the formation of copper oxide nanoparticles were responsible for the darkening of the MOF color (Figure S1). The darkening of the MOF-199 color has been reported in the literature, where the Cu coordination number changes from six to five after the removal of coordinated water or the solvent from the Cu sites.[43] The third region in MOF-199-A has the same feature as that observed for MOF-199. The final weight of 24.7% in MOF-199-A as opposed to 20.7% in MOF-199 confirmed the oxide formation even at 200 °C. The TGA profile of CuO-280 has a slight weight loss in the 300−600 °C zone due to the presence of residual carbon. Wang et al. reported the fabrication of Cu_2O/CuO from the calcination of MOF-199 at 300 °C. At 300 °C, the oxide products have 0.20−2.26% remnant carbon.[42] CuO-550 showed no weight loss in the entire temperature profile, which validated the complete conversion of MOF-199 to CuO.

The XPS full-scan survey of MOF-199 and calcined products is shown in Figure S6. All the samples have peaks for C 1s, O 1s, and Cu 2p at their respective binding energy. With the calcination temperature, the Cu 2p peak intensity increased at the expense of the C 1s peak, showing the oxidation of the organic linker. The presence of the C 1s peak in the CuO-550 was due to the adventitious carbon. The HRXPS Cu 2p spectra of the MOF and calcined products are shown in Figure 3, and

https://doi.org/10.1021/acsomega.1c03712
ACS Omega 2021, 6, 25631−25641

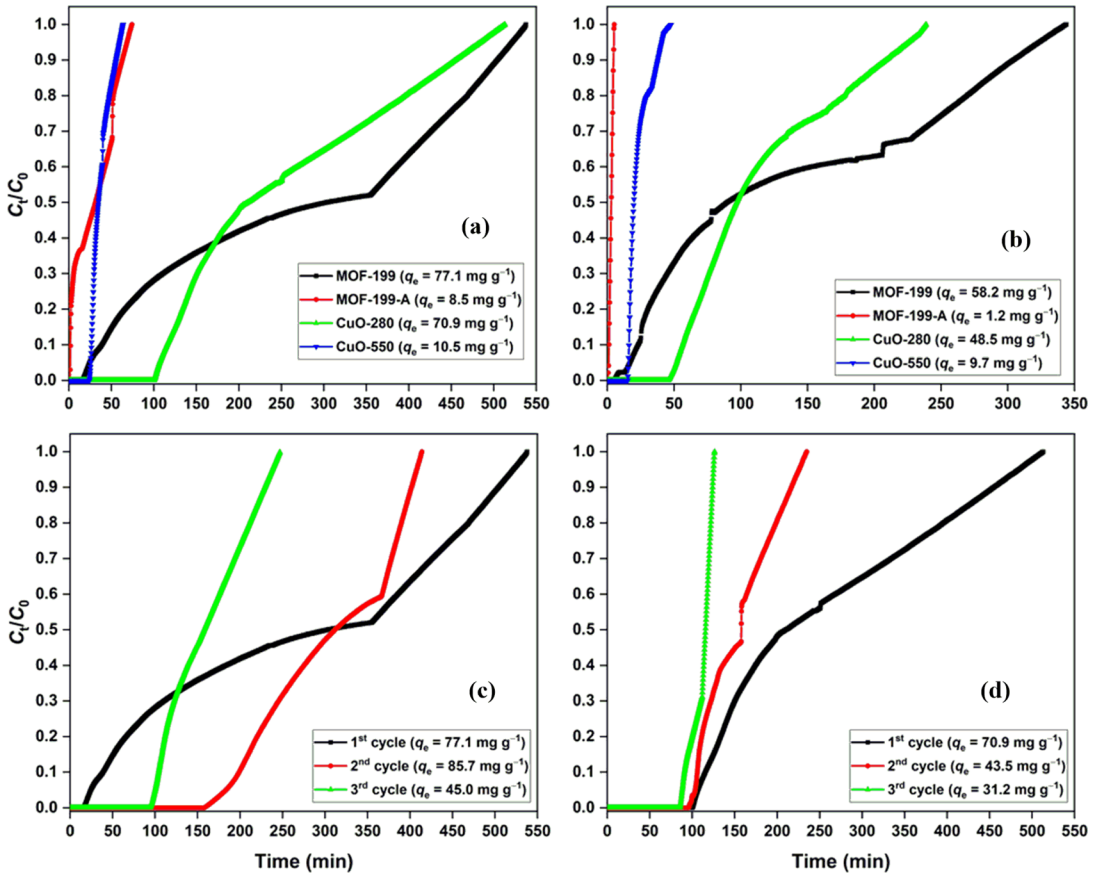

Figure 4. H_2S breakthrough curves with (a) 0.2 L min^{-1}, (b) 0.3 L min^{-1}, (c) MOF-199 regeneration, and (d) CuO-280 regeneration with a 0.2 L min^{-1} flow rate.

fitting parameters are listed in Table S3. The HRXPS Cu spectrum of MOF-199 has peaks at 934.4 and 954.3 eV for Cu $2p_{3/2}$ and Cu $2p_{1/2}$, respectively, with multiple satellite peaks. Based on the peak positions, the peaks mainly originated from Cu^{2+} and not Cu^{+} as XPS Cu^{2+} peaks usually appear at a higher energy.[44] The Cu $2p_{3/2}$ peak was deconvoluted into two contributions at 932.3 (16.5%) and 934.5 eV (83.5%) for Cu^{+} and Cu^{2+} sites, respectively.[21,26] Multiple peaks located at 947−938 and 958−965 eV were shake-up satellites for Cu^{2+} sites. These satellite peaks are due to the $\vec{p}d$ hybridization occurring when the Cu electronic configuration is unsaturated (d^9) and absent in the Cu^{+} oxidation state (d^{10}) (Figure 3a).[45] In MOF-199-A, a large fraction of the Cu^{+} sites oxidized to Cu^{2+}, and the remaining Cu^{+} accounted for 9.5% of the total Cu sites (Figure 3b). The HRXPS Cu 2p spectrum of CuO-280 has peaks at 933.4 and 953.3 eV for Cu $2p_{3/2}$ and Cu $2p_{1/2}$, respectively. The binding energy lowered by 1.0 eV compared to MOF-199. The decreased binding energy was due to the reduction of Cu^{2+} sites to Cu^{+} after calcination at 280 °C. The Cu $2p_{3/2}$ peak of CuO-280 has contributions at 933.2 (61.3%) and 934.7 eV (38.7) for Cu^{+} and Cu^{2+}, respectively. The larger contribution from Cu^{+} in CuO-280 after air calcination has been reported in the literature as well.[42] Though the PXRD analysis predicted Cu_2O in CuO-280, the proportion was not enough to account for such a large Cu^{+} density. Thus, it was obvious that a significant proportion of Cu^{+} sites along with oxygen vacancies (O_v) were present in CuO. For every O atom that is removed from the lattice, two electrons are left behind, which reduces two Cu^{2+} sites to two Cu^{+} sites (Figure 3c).[46] The deconvolution of the HRXPS Cu $2p_{3/2}$ peak of CuO-550 had similar peak positions as observed in CuO-280. Here, the Cu^{+} and Cu^{2+} accounted for 56.4 and 43.6% of the total Cu content. Since the PXRD pattern of CuO-550 confirmed the absence of the Cu_2O phase, the entire Cu^{+} was linked to CuO with O_v (Figure 3d).

The HRXPS O 1s spectra of MOF-199 and calcined products are shown in Figure S7, and fitting parameters are listed in Table S4. The HRXPS O 1s spectrum of MOF-199 fitted into three contributions at 531.5, 532.9, and 533.7 eV for Cu−O, C−O, and H_2O, respectively (Figure S7a).[47] The HRXPS O 1s spectrum of MOF-199-A has similar contributions, with the binding energy shifting to a lower value for all three peaks. The binding energies of Cu−O and C−O peaks shifted to 531.1 and 531.8 eV, respectively (Figure S7b). In general, the O 1s peak for the lattice O^{2-} in CuO/Cu_2O is observed at ∼529.6−530.3 eV.[48] Moreover, the peak for oxygen vacancy is reported at ∼531.7 eV.[49] The initial formation of oxide nanoparticles shifted the binding energy of both peaks to a lower value. Thus, tracing these two peaks is sufficient to confirm the oxide growth with increasing calcination temperature. The HRXPS O 1s spectrum of CuO-280 has a major shift in the binding energy of the Cu−O peak from 531.1 (in MOF-199-A) to 530.0 eV (Figure S7c). The value of 530.0 eV is the standard binding energy for Cu−O bonds in the metal oxide. Moreover, the contribution from the 531.8 eV peak in MOF-199-A decreased from 52.0 to 27.7% in CuO-280. Thus, 280 °C was the transition temperature where most of the carbon oxidized. The 531.7

https://doi.org/10.1021/acsomega.1c03712
ACS Omega 2021, 6, 25631−25641

eV peak was assigned to the O_v (27.7%).[42] The HRXPS O 1s spectrum of CuO-550 showed no further shift in the binding energy, except for slight variation in the Cu−O and O_v contributions (Figure S7d). The Cu−O contribution decreased by 0.8% due to the oxidation of Cu_2O, whereas the O_v contribution increased by 2.7% due to O_v formation at elevated temperatures. The HRXPS C 1s spectra of MOF-199 and calcined products are shown in Figure S8. In the HRXPS C 1s spectra of MOF-199 and MOF-199-A, two distinct features at 284.7 and 288.7 eV were assigned to the C═C and O−C═O bonds, respectively.[50] These peaks started fading with the increasing temperature of CuO-280 and CuO-550. The observed 284.7 eV peak in oxide samples was due to the adventitious carbon.

H_2S Breakthrough Studies. The H_2S breakthrough curves for fresh adsorbents with different flow rates are shown in Figure 4a,b. The adsorption capacity followed the trend MOF-199 (77.1 mg g^{-1}) > CuO-280 (70.9 mg g^{-1}) > CuO-550 (10.5 mg g^{-1}) > MOF-199-A (8.5 mg g^{-1}) with a flow rate of 0.2 L min^{-1} (Figure 4a). Though the trend observed at 0.2 L min^{-1} was unaltered, the adsorption capacity decreased when the flow rate increased to 0.3 L min^{-1} (Figure 4b). The adsorbate−adsorbent interaction (adsorption capacity) depends on the retention time of gas molecules in the adsorbent bed. Increasing the flow rate lowers the retention time, i.e., H_2S molecules have lesser time to diffuse into the MOF pores, which limits the adsorbate−adsorbent interaction.[26] In our previous work on the chemisorption of H_2S over MOF-199, the maximum adsorption capacity of 27.1 mg g^{-1} was achieved even with a higher surface area of 317.0 m^2 g^{-1}.[21] In the present work, the surface area of MOF-199 is comparatively low (231.9 m^2 g^{-1}). The higher adsorption capacity in this work was largely due to a high pore volume (nearly 3.5 times higher than the previously reported one). Bhoria et al. reported the maximum adsorption capacity of 52.8 mg g^{-1} for MOF-199 with a surface area of 1380.0 m^2 g^{-1}.[18] Thus, the synthesized microrod MOF-199 has superior adsorption capacity compared to the previously reported MOF-199.

Though numerous studies are dedicated to the removal of H_2S over MOF-199-based adsorbents, regeneration of spent MOF-199 is largely unexplored in the literature. Even among numerous adsorbents reported for room-temperature H_2S removal, only a handful of studies have addressed the reusability for multiple cycles (Table S5). In the present work, we have reported heating at 70 °C for 2 days as the regeneration method. The photographic images of regenerated MOF-199 at different stages are shown in Figure S9. The breakthrough curves for regenerated MOF-199 and CuO-280 are shown in Figure 4c,d, respectively. The adsorption capacity of 85.7 mg g^{-1} in the second cycle was an improvement over the first cycle. Meanwhile, the adsorption capacity decreased to 45.0 mg g^{-1} in the third cycle. Previously, we reported the regeneration of MOF-199 using a novel methanol/UV irradiation method, which increased the adsorption capacity of MOF-199 by 3.5 times in the second cycle.[21] For CuO-280, the adsorption capacity decreased with the increasing number of adsorption−regeneration cycles. In the regeneration studies, MOF-199 outperformed CuO-280 in all three cycles. The regeneration was tested for only three cycles as the trend was obvious, and the samples were labeled as exhausted adsorbents. These exhausted adsorbents were tested as photocatalysts for the degradation of the MB dye.

The H_2S adsorption capacity of adsorbents was correlated with their physicochemical properties (Figure 5). The trend

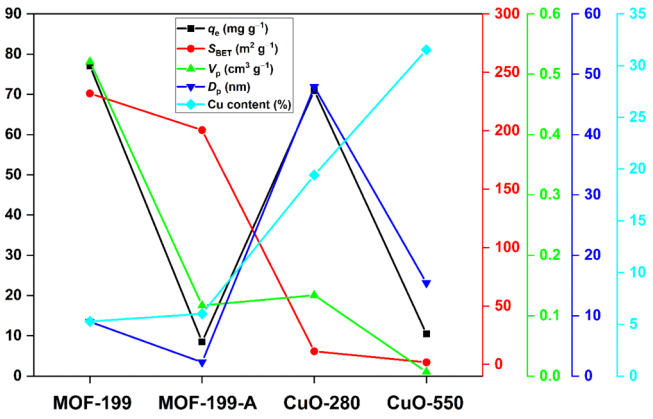

Figure 5. Adsorption capacity relationship with adsorbent properties.

followed by the adsorption capacity (MOF-199 > CuO-280 > CuO-550 > MOF-199-A) did not fully incline with any of the properties. The maximum adsorption capacity of MOF-199 was due to the highest surface area. Though MOF-199-A also possessed a high surface area, the adsorption capacity was the lowest and was linked to its decreased pore volume. Thus, for MOF-199 and MOF-199-A, the surface area and the pore volume played a decisive role in H_2S removal. Between CuO-280 and CuO-550, CuO-280 performed better due to its superior surface area and pore properties. For all four adsorbents, the adsorption process was largely driven by the pore characteristics.

Adsorption Mechanism. The PXRD patterns of fresh and spent MOF-199 are shown in Figure 6a. In the literature, multiple studies are focused on H_2S removal using MOF-199.[19,21,51] Ethiraj et al. reported the destruction of the MOF framework upon H_2S exposure with the formation of a CuS phase.[25] Ebrahim et al. confirmed Cu_2S, CuS, Cu_2SO_4, and $CuSO_3$ in the MOF-199/GO composite after H_2S exposure with a partial loss in the MOF crystallinity.[20] In our previously published work, we also observed partial destruction of the MOF framework. However, this effect was not accompanied by the formation of CuS or any other Cu sulfite and sulfate phases.[21] In the present study, the diffraction pattern of spent MOF overlapped with the fresh one with an insignificant loss in intensity. Moreover, peaks corresponding to the CuS phase were absent.[52] Thus, H_2S molecules may have interacted with the Cu sites without significant cleaving of Cu−O bonds. Thus, unlike other published reports, we have observed the high stability of MOF-199 upon H_2S exposure. The PXRD patterns of fresh and spent CuO-280 are shown in Figure 6b. Both the patterns are nearly identical, where CuS/Cu_2S phases were absent.

In the FTIR spectrum of spent MOF-199, two new bands observed at 620 and 1110 cm^{-1} were assigned to the out-of-plane bending and symmetric stretching vibration of SO_4^{2-}, respectively (Figure 6c).[53,54] The bands corresponding to the MOF framework were largely intact with decreased intensity for 1655 cm^{-1} (carboxylate groups in larger pores). The decreased intensity of this band hinted toward the protonation of the carboxylate after H_2S interaction with the Cu sites.[55] The FTIR spectrum of spent CuO-280 has a new high-intensity band at 1110 cm^{-1} for sulfates (Figure 6d). The band

https://doi.org/10.1021/acsomega.1c03712
ACS Omega 2021, 6, 25631−25641

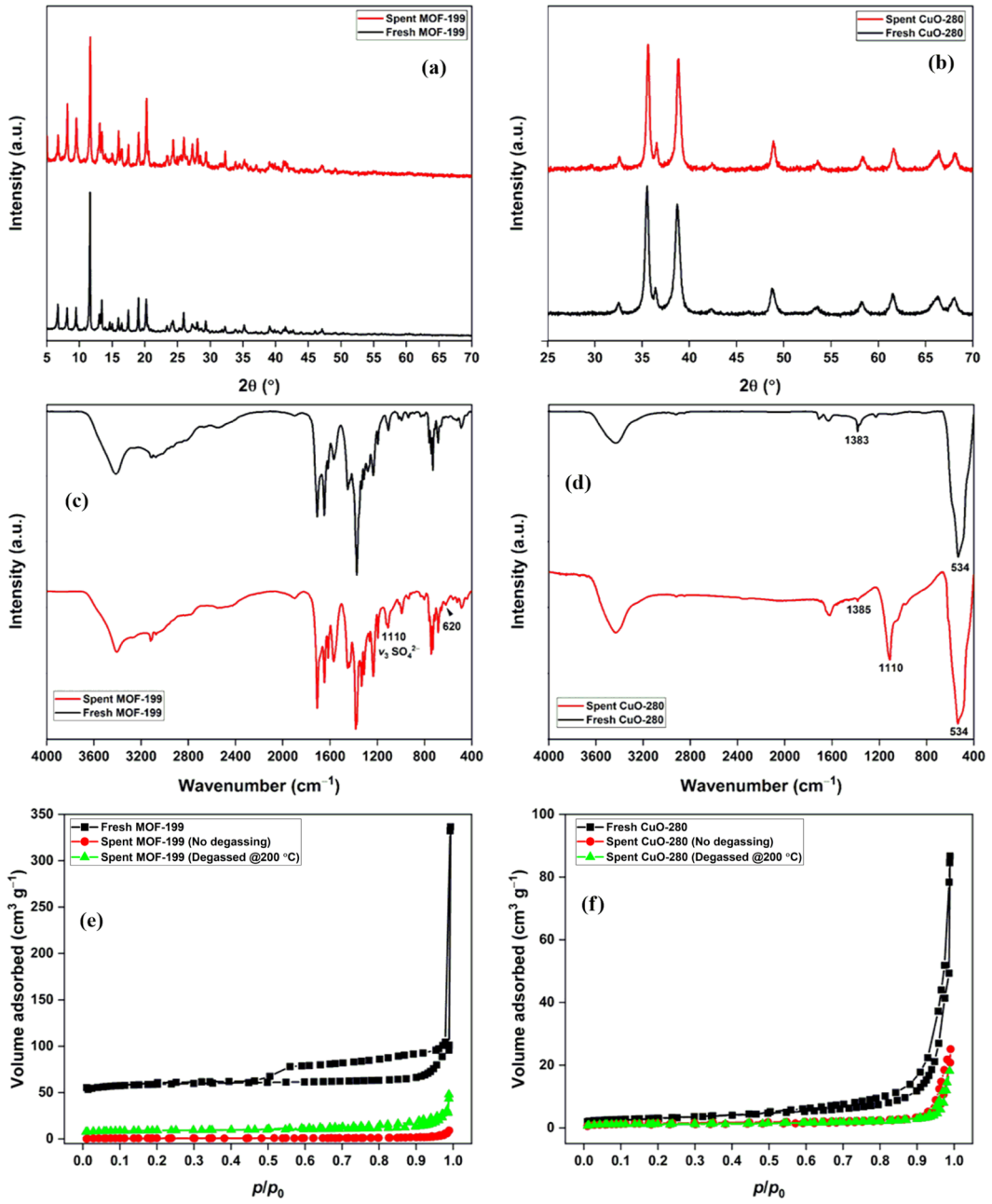

Figure 6. PXRD patterns of (a) MOF-199 and (b) CuO-280, FTIR spectra of (c) MOF-199 and (d) CuO-280, and N_2 adsorption−desorption isotherms of (e) MOF-199 and (f) CuO-280 before and after H_2S exposure.

for Cu−O was at the same wavenumber even in the spent CuO-280. Thus, the desulfurization process over MOF-199 and CuO-280 was driven by the conversion of H_2S to SO_4^{2-} species. The N_2 adsorption−desorption isotherms of fresh and spent MOF-199 and CuO-280 are given in Figure 6e,f, respectively. The surface area of the spent MOF-199 without degassing was 2.87 m^2 g^{-1}, which increased to 34.40 m^2 g^{-1} after degassing of the sample at 200 °C. The increased surface area after degassing was probably due to the removal of axially coordinated H_2S/H_2O molecules. The decrease in the surface area of MOF-199 after H_2S exposure is well-documented in the literature.[21,51] The surface area of spent CuO-280 before degassing was 5.37 m^2 g^{-1}, which reached 4.74 m^2 g^{-1} after the degassing process. The decreased surface area of spent CuO-280 was due to the formation of sulfate species, which blocked the pores (Table S6).

Repurposing Exhausted Adsorbents. The FTIR spectra of exhausted MOF-199 and CuO-280 are shown in Figure 7a. The FTIR spectrum of exhausted CuO-280 has two new bands at 620 and 1110 cm^{-1} for SO_4^{2-} species. The bands around 400−600 cm^{-1} were assigned to the Cu−O/Cu−S stretching vibrations.[56] The FTIR spectrum of exhausted MOF-199 has bands at 620 and 1110 cm^{-1} for sulfates. Bands at 2551 and 2664 cm^{-1} were assigned to the S−H stretching vibrations.[57] The doublet at 1709 and 1655 cm^{-1} assigned to the carboxylate group (in the large pores of the fresh MOF-199) framework shifted to 1719 and 1610 cm^{-1} due to the cleaving of the Cu−carboxylate bond to form −COOH groups (Figure S10).[55] The PXRD patterns of exhausted adsorbents are shown

https://doi.org/10.1021/acsomega.1c03712
ACS Omega 2021, 6, 25631−25641

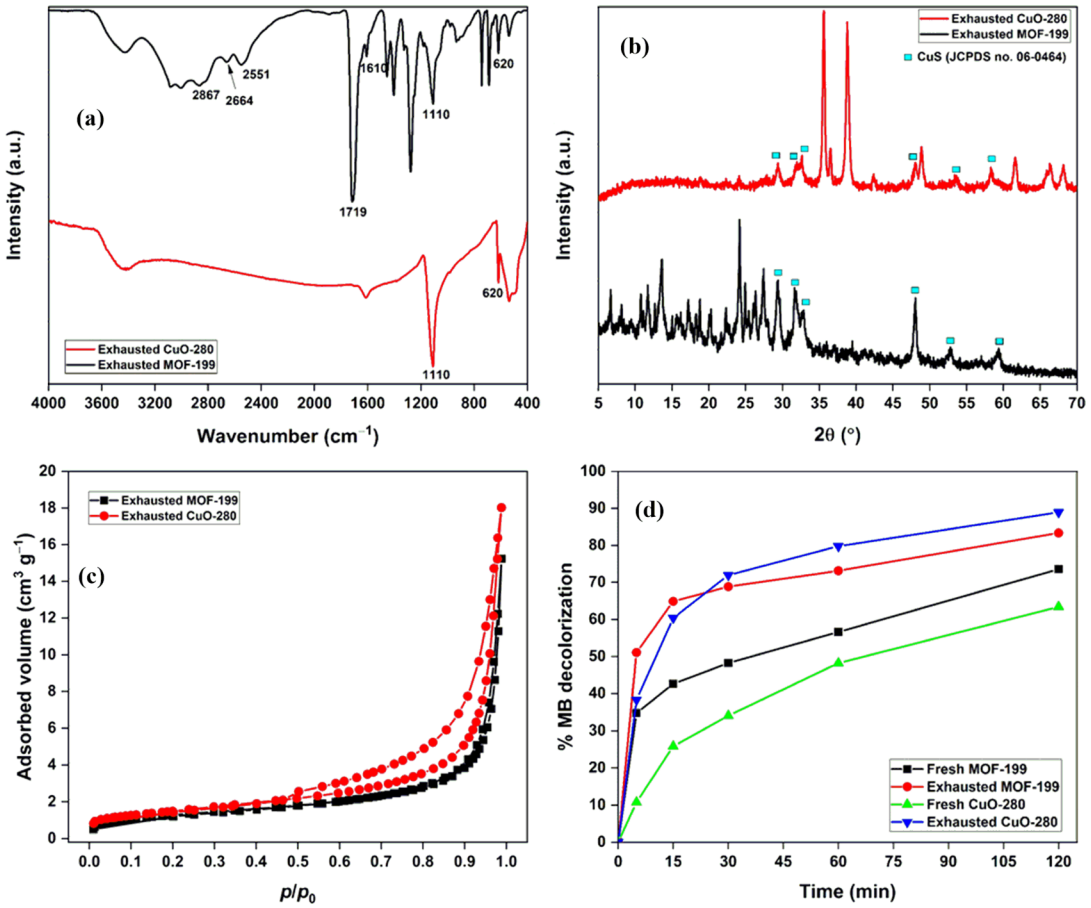

Figure 7. (a) FTIR spectra, (b) PXRD patterns, and (c) N_2 adsorption−desorption isotherms of exhausted adsorbents; (d) photocatalytic degradation of the MB dye in a H_2O_2/UV system. Conditions: [MB] = 10 mg L^{-1}, [photocatalyst] = 1.0 g L^{-1}, and [H_2O_2] = 20 mmol L^{-1}.

in Figure 7b. In the PXRD pattern of exhausted MOF-199, the peak intensity for the MOF decreased with the appearance of new peaks (ocean blue square) for CuS covellite (JCPDS no. 06-0464).[52] In the exhausted CuO-280, the peaks for CuO and Cu_2O were intact with the appearance of new peaks for CuS covellite. The N_2 adsorption−desorption isotherms of exhausted MOF-199 and CuO-280 are shown in Figure 7c. The surface area of exhausted MOF-199 (4.74 m^2 g^{-1}) was found to be considerably lower than that of the spent MOF-199 (34.40 m^2 g^{-1}). MOF-199 exposure to the three runs of H_2S gas deteriorated the MOF structure. The surface area of exhausted CuO-280 was 5.39 m^2 g^{-1}, which was slightly higher than that of the spent CuO-280 (Table S6).

The exhausted adsorbents were repurposed for the photocatalytic degradation of the MB dye in the H_2O_2/UV system. In the literature, MOF-199 and CuO have been studied for the removal of organic dyes.[58,59] Similarly, CuS and CuS/CuO have been reported as efficient photocatalysts for water decolorization.[60−62] The exhausted MOF-199 and CuO-280 have sulfide species bound to the Cu sites. Though these materials could not be used for the desulfurization process after multiple cycles, these sulfur-rich exhausted materials could be excellent photocatalysts for the degradation of organic dyes in colored wastewater. Thus, the repurposing of exhausted adsorbents has been tested by degrading the MB dye in a 32 W UV-assisted photo-Fenton process (Figure 7d). The decolorization efficiencies of fresh MOF-199 and CuO-280 after 2 h were 73.6 and 63.4%, respectively. Meanwhile, for exhausted MOF-199 and CuO-280, the efficiencies were 83.4 and 89.0%, respectively. In the literature, numerous studies are dedicated to the modification of photocatalytic properties of the material by incorporating nonmetals as dopants. Pillai et al. reported improved photocatalytic degradation of organic pollutants over S-doped TiO_2 compared to TiO_2. The insertion of sulfur as sulfide in the TiO_2 lattice lowered the bandgap energy and weakened the charge carrier recombination rate.[63] Devi and Kavitha reported improved phenol photodegradation over S-TiO_2 compared to TiO_2. Here, sulfur as sulfate ions increased the UV-photon absorption, decreased bandgap energy, and quenched the charge recombination process by acting as electron traps.[64] This behavior has been observed in CuO and CuO−CuS photocatalysts as well, where the CuO−CuS photocatalyst showed better MB degradation efficacy.[62] Here, sulfur was present as sulfide and sulfate in the exhausted adsorbents, which improved their photocatalytic activity.

CONCLUSIONS

In this study, we report the fabrication of MOF-199 microrods and their thermal transformation into CuO nanoparticles. The transformation process was probed through various microscopic and spectroscopic techniques. The oxide growth was initiated by ∼2.5 nm seed formation at 200 °C, which increased to ∼10 nm at 280 °C and ∼100−250 nm at 550 °C. HRTEM and PXRD confirmed an intermediate presence of Cu_2O at 280 °C. BET and FTIR analysis confirmed the partial

https://doi.org/10.1021/acsomega.1c03712
ACS Omega 2021, 6, 25631−25641

collapse of larger pores at 200 °C. The MOF and calcined products were studied for H_2S removal in ambient conditions. Among adsorbents studied, MOF-199 showed the maximum adsorption capacity of 77.1 mg g^{-1} followed by CuO-280 (70.9 mg g^{-1}). Spent MOF-199 and CuO-280 were effectively regenerated by thermal heating at 70 °C. Here also, MOF-199 showed a better regeneration efficiency than the oxide product. As a sustainable approach, the exhausted adsorbents were studied as photocatalysts for the degradation of methylene blue. The exhausted materials showed better degradation efficiencies than the fresh materials. This study reports one of the few methods developed for MOF regeneration. Moreover, we have proposed an alternative and green approach for the secondary use of exhausted adsorbents.

EXPERIMENTAL SECTION

Chemicals. Copper(II) nitrate trihydrate ($Cu(NO_3)_2 \cdot 3H_2O$, purity >98%), benzene-1,3,5-tricarboxylic acid (H_3BTC, purity of >95%), and the MB dye were purchased from Sigma Aldrich, Germany. *N*,*N*-dimethylformamide (DMF, purity of >99%) and hydrogen peroxide (28% H_2O_2) solution were purchased from Samchun Pure Chemicals, Korea. Pure H_2S gas (500 ppm balanced with N_2 gas) was procured from Union Gas, Korea.

Synthesis of Adsorbents. MOF-199 microrods were synthesized in a 2.5 L batch reactor at room temperature. The ligand solution was prepared by dissolving 42.0 g of H_3BTC in 0.5 L of DMF. The copper solution was prepared by dissolving 72.5 g of $Cu(NO_3)_2 \cdot 3H_2O$ in 2 L of deionized water. The ligand solution was added to the copper salt solution under rapid stirring. After 1 h of stirring, the suspension was left for 48 h followed by phase separation and drying of the precipitate at 70 °C in a hot-air oven. MOF-199 was heated at 200, 280, and 550 °C for 8 h to yield MOF-199-A, CuO-280, and CuO-550, respectively. The photographic images of MOF-199 and calcined products are shown in Figure S1.

Instruments. Information on analytical instruments is available in Section S1.

Experimental Procedures. *H_2S Breakthrough Curves.* A 0.5 g mass of a powdered sample was placed in between glass wool in a Pyrex tube (height of 50 cm, diameter of 1 cm) supported on silica beads. The H_2S gas (500 ppm) was passed through it at a fixed flow rate at 25 °C. The outgoing gas was analyzed by a gas analyzer (GSR-310, Sensoronic, Korea) every 15 s until the effluent concentration reached 500 ppm. The adsorption capacity (q, mg g^{-1}) at the breakthrough point was calculated by integration of the area above the curve (eq 1).

$$q = \frac{C_0 Q}{m} \int_0^{t_b} \left(1 - \frac{C}{C_0}\right) dt \quad (1)$$

C_0 is the initial concentration (500 ppm or 0.697 mg L^{-1}), Q is the flow rate, m is the mass of the MOF (g), and t_b is the breakthrough time.

H_2S Regeneration Study. The spent sample in a closed glass vial was kept in a hot-air oven at 70 °C for 2 days. The regenerated sample was repacked in the column, and H_2S breakthrough curves were recorded.

Photocatalytic Study. The photocatalytic performance of fresh and exhausted samples was evaluated by degrading the MB dye. Exactly, 100 mg of material and 0.2 mL of 28% H_2O_2 solution were added in 100 mL of MB dye solution (10 mg L^{-1}) in a 250 mL Pyrex glass tube. The Pyrex tube was placed in an acrylic reactor with four UV lamps (8 W, I_{max} of ~254 nm, Philips, The Netherlands). All the experiments were performed at 20 ± 2 °C (temperature was maintained by cooling fans) and at neutral pH. After a fixed time, 2 mL of the aqueous phase was taken out with a disposable syringe filter (Hyundai Micro, Model SN25P045NS, pore size of 0.45 μm) to lock the material. After suitable dilution, the aqueous sample was analyzed by UV−vis spectroscopy (LAMBDA 365 UV/vis spectrophotometer, PerkinElmer) at λ_{max} = 664 nm.

ASSOCIATED CONTENT

Supporting Information

The Supporting Information is available free of charge at https://pubs.acs.org/doi/10.1021/acsomega.1c03712.

Photographic image, TEM-EDAX analysis, FTIR spectra, XPS and HRXPS O 1s and C 1s spectra of fresh adsorbents, photographic images of spent and regenerated adsorbents, FTIR spectrum of the H_3BTC ligand, listing of the atomic composition of adsorbents, surface and pore characteristics, XPS curve fitting parameters, and adsorption capacity and regenerability of reported adsorbents (PDF)

AUTHOR INFORMATION

Corresponding Author

Jiyeol Bae − *University of Science and Technology (UST), Daejeon 34113, Republic of Korea; Department of Land, Water, and Environment Research, Korea Institute of Civil Engineering and Building Technology (KICT), Goyang 10223, Republic of Korea;* orcid.org/0000-0001-6119-9349; Email: baejiyeol@kict.re.kr

Authors

Nishesh Kumar Gupta − *University of Science and Technology (UST), Daejeon 34113, Republic of Korea; Department of Land, Water, and Environment Research, Korea Institute of Civil Engineering and Building Technology (KICT), Goyang 10223, Republic of Korea*

Kwang Soo Kim − *University of Science and Technology (UST), Daejeon 34113, Republic of Korea; Department of Land, Water, and Environment Research, Korea Institute of Civil Engineering and Building Technology (KICT), Goyang 10223, Republic of Korea*

Complete contact information is available at: https://pubs.acs.org/10.1021/acsomega.1c03712

Author Contributions

The manuscript was written through the contributions of all authors. All authors have approved the final version of the manuscript.

Notes

The authors declare no competing financial interest.

ACKNOWLEDGMENTS

The authors are very grateful for the funds [project no. 20210152-001] provided by the "Korea Institute of Civil Engineering and Building Technology" (KICT), Republic of Korea.

REFERENCES

(1) Shekhah, O.; Liu, J.; Fischer, R. A.; Wöll, C. MOF thin films: Existing and future applications. *Chem. Soc. Rev.* **2011**, *40*, 1081−1106.

(2) Sumida, K.; Rogow, D. L.; Mason, J. A.; McDonald, T. M.; Bloch, E. D.; Herm, Z. R.; Bae, T.-H.; Long, J. R. Carbon Dioxide Capture in Metal−Organic Frameworks. *Chem. Rev.* **2012**, *112*, 724−781.

(3) Rieth, A. J.; Wright, A. M.; Dincă, M. Kinetic stability of metal−organic frameworks for corrosive and coordinating gas capture. *Nat. Rev. Mater.* **2019**, *4*, 708−725.

(4) López, Y. C.; Viltres, H.; Gupta, N. K.; Acevedo-Peña, P.; Leyva, C.; Ghaffari, Y.; Gupta, A.; Kim, S.; Bae, J.; Kim, K. S. Transition metal-based metal−organic frameworks for environmental applications: A review. *Environ. Chem. Lett.* **2021**, *19*, 1295−1334.

(5) Gao, M.-L.; Wang, W.-J.; Liu, L.; Han, Z.-B.; Wei, N.; Cao, X.-M.; Yuan, D.-Q. Microporous Hexanuclear Ln(III) Cluster-Based Metal−Organic Frameworks: Color Tunability for Barcode Application and Selective Removal of Methylene Blue. *Inorg. Chem.* **2017**, *56*, 511−517.

(6) Kuyuldar, S.; Genna, D. T.; Burda, C. On the potential for nanoscale metal−organic frameworks for energy applications. *J. Mater. Chem. A* **2019**, *7*, 21545−21576.

(7) Zhang, Y.; Wang, Y.; Liu, L.; Wei, N.; Gao, M.-L.; Zhao, D.; Han, Z.-B. Robust Bifunctional Lanthanide Cluster Based Metal−Organic Frameworks (MOFs) for Tandem Deacetalization−Knoevenagel Reaction. *Inorg. Chem.* **2018**, *57*, 2193−2198.

(8) Wang, J.; Luo, X.; Young, C.; Kim, J.; Kaneti, Y. V.; You, J.; Kang, Y.-M.; Yamauchi, Y.; Wu, K. C.-W. A Glucose-Assisted Hydrothermal Reaction for Directly Transforming Metal−Organic Frameworks into Hollow Carbonaceous Materials. *Chem. Mater.* **2018**, *30*, 4401−4408.

(9) Gupta, N. K.; Bae, J.; Kim, K. S. Metal-organic framework-derived $NaMn_xO_y$ hexagonal microsheets for superior adsorptive-oxidative removal of hydrogen sulfide in ambient conditions. *Chem. Eng. J.* **2022**, *427*, 130909.

(10) Singh, C.; Mukhopadhyay, S.; Hod, I. Metal−organic framework derived nanomaterials for electrocatalysis: Recent developments for CO_2 and N_2 reduction. *Nano Convergence* **2021**, *8*, 1.

(11) Wang, Q.; Astruc, D. State of the Art and Prospects in Metal−Organic Framework (MOF)-Based and MOF-Derived Nanocatalysis. *Chem. Rev.* **2020**, *120*, 1438−1511.

(12) Koo, W.-T.; Jang, J.-S.; Kim, I.-D. Metal-Organic Frameworks for Chemiresistive Sensors. *Chem* **2019**, *5*, 1938−1963.

(13) Gupta, N. K.; Bae, J.; Kim, K. S. Metal organic framework derived $NaCo_xO_y$ for room temperature hydrogen sulfide removal. *Sci. Rep.* **2021**, *11*, 14740.

(14) Hiraide, S.; Sakanaka, Y.; Kajiro, H.; Kawaguchi, S.; Miyahara, M. T.; Tanaka, H. High-throughput gas separation by flexible metal−organic frameworks with fast gating and thermal management capabilities. *Nat. Commun.* **2020**, *11*, 3867.

(15) Denning, S.; Majid, A. A.; Lucero, J. M.; Crawford, J. M.; Carreon, M. A.; Koh, C. A. Metal−Organic Framework HKUST-1 Promotes Methane Hydrate Formation for Improved Gas Storage Capacity. *ACS Appl. Mater. Interfaces* **2020**, *12*, 53510−53518.

(16) Pokhrel, J.; Bhoria, N.; Wu, C.; Reddy, K. S. K.; Margetis, H.; Anastasiou, S.; George, G.; Mittal, V.; Romanos, G.; Karonis, D.; Karanikolos, G. N. Cu- and Zr-based metal organic frameworks and their composites with graphene oxide for capture of acid gases at ambient temperature. *J. Solid State Chem.* **2018**, *266*, 233−243.

(17) Supronowicz, B.; Mavrandonakis, A.; Heine, T. Interaction of Small Gases with the Unsaturated Metal Centers of the HKUST-1 Metal Organic Framework. *J. Phys. Chem. C* **2013**, *117*, 14570−14578.

(18) Bhoria, N.; Basina, G.; Pokhrel, J.; Kumar Reddy, K. S.; Anastasiou, S.; Balasubramanian, V. V.; AlWahedi, Y. F.; Karanikolos, G. N. Functionalization effects on HKUST-1 and HKUST-1/graphene oxide hybrid adsorbents for hydrogen sulfide removal. *J. Hazard. Mater.* **2020**, *394*, 122565.

(19) Lee, M.-H.; Vikrant, K.; Younis, S. A.; Szulejko, J. E.; Kim, K.-H. Chemisorption of hydrogen sulfide by metal-organic frameworks and covalent-organic polymers based on experimental/theoretical evaluation. *J. Cleaner Prod.* **2020**, *250*, 119486.

(20) Ebrahim, A. M.; Jagiello, J.; Bandosz, T. J. Enhanced reactive adsorption of H_2S on Cu−BTC/S- and N-doped GO composites. *J. Mater. Chem. A* **2015**, *3*, 8194−8204.

(21) Gupta, N. K.; Kim, S.; Bae, J.; Kim, K. S. Chemisorption of hydrogen sulfide over copper-based metal−organic frameworks: Methanol and UV-assisted regeneration. *RSC Adv.* **2021**, *11*, 4890−4900.

(22) Yang, Y.; Dong, H.; Wang, Y.; Wang, Y.; Liu, N.; Wang, D.; Zhang, X. A facile synthesis for porous CuO/Cu_2O composites derived from MOFs and their superior catalytic performance for CO oxidation. *Inorg. Chem. Commun.* **2017**, *86*, 74−77.

(23) Tran, T. V.; Nguyen, D. T. C.; Nguyen, T. T.; Le, H. T. N.; Nguyen, C. V.; Nguyen, T. D. Metal-organic framework HKUST-1-based $Cu/Cu_2O/CuO@C$ porous composite: Rapid synthesis and uptake application in antibiotics remediation. *J. Water, Process Eng.* **2020**, *36*, 101319.

(24) Zamaro, J. M.; Pérez, N. C.; Miró, E. E.; Casado, C.; Seoane, B.; Téllez, C.; Coronas, J. HKUST-1 MOF: A matrix to synthesize CuO and $CuO−CeO_2$ nanoparticle catalysts for CO oxidation. *Chem. Eng. J.* **2012**, *195-196*, 180−187.

(25) Ethiraj, J.; Bonino, F.; Lamberti, C.; Bordiga, S. H_2S interaction with HKUST-1 and ZIF-8 MOFs: A multitechnique study. *Microporous Mesoporous Mater.* **2015**, *207*, 90−94.

(26) Gupta, N. K.; Kim, S.; Bae, J.; Soo Kim, K. Fabrication of $Cu(BDC)_{0.5}(BDC\text{-}NH_2)_{0.5}$ metal-organic framework for superior H_2S removal at room temperature. *Chem. Eng. J.* **2021**, *411*, 128536.

(27) He, D.; Zhang, Y.; Yang, S.; Zhang, L.; Lu, J.; Zhao, Y.; Mei, Y.; Han, C.; Luo, Y. Development of a Strategy To Reuse Spent Cr Adsorbents as Efficient Catalysts: From the Perspective of Practical Application. *ACS Sustainable Chem. Eng.* **2019**, *7*, 3251−3257.

(28) Umejuru, E. C.; Prabakaran, E.; Pillay, K. Coal fly ash coated with carbon hybrid nanocomposite for remediation of cadmium (II) and photocatalytic application of the spent adsorbent for reuse. *Results Mater.* **2020**, *7*, 100117.

(29) Mazaj, M.; Čendak, T.; Buscarino, G.; Todaro, M.; Zabukovec Logar, N. Confined crystallization of a HKUST-1 metal−organic framework within mesostructured silica with enhanced structural resistance towards water. *J. Mater. Chem. A* **2017**, *5*, 22305−22315.

(30) Feng, Y.; Li, Z.; Liu, H.; Dong, C.; Wang, J.; Kulinich, S. A.; Du, X. Laser-Prepared CuZn Alloy Catalyst for Selective Electrochemical Reduction of CO_2 to Ethylene. *Langmuir* **2018**, *34*, 13544−13549.

(31) Chen, K.; Ling, J.; Wu, C. In Situ Generation and Stabilization of Accessible Cu/Cu_2O Heterojunctions inside Organic Frameworks for Highly Efficient Catalysis. *Angew. Chem., Int. Ed.* **2020**, *59*, 1925−1931.

(32) Horiuchi, S.; Hanada, T.; Ebisawa, M.; Matsuda, Y.; Kobayashi, M.; Takahara, A. Contamination-Free Transmission Electron Microscopy for High-Resolution Carbon Elemental Mapping of Polymers. *ACS Nano* **2009**, *3*, 1297−1304.

(33) Todaro, M.; Buscarino, G.; Sciortino, L.; Alessi, A.; Messina, F.; Taddei, M.; Ranocchiari, M.; Cannas, M.; Gelardi, F. M. Decomposition Process of Carboxylate MOF HKUST-1 Unveiled at the Atomic Scale Level. *J. Phys. Chem. C* **2016**, *120*, 12879−12889.

(34) Schlichte, K.; Kratzke, T.; Kaskel, S. Improved synthesis, thermal stability and catalytic properties of the metal-organic framework compound $Cu_3(BTC)_2$. *Microporous Mesoporous Mater.* **2004**, *73*, 81−88.

(35) Mall, A. K.; Kumar, P.; Garg, A.; Gupta, R. Synthesis, growth, and characterizations of CuO single crystal. *AIP Conf. Proc.* **2018**, *1953*, No. 070008.

(36) Markose, K. K.; Shaji, M.; Bhatia, S.; Nair, P. R.; Saji, K. J.; Antony, A.; Jayaraj, M. K. Novel Boron-Doped p-Type Cu_2O Thin Films as a Hole-Selective Contact in c-Si Solar Cells. *ACS Appl. Mater. Interfaces* **2020**, *12*, 12972−12981.

https://doi.org/10.1021/acsomega.1c03712
ACS Omega 2021, 6, 25631−25641

(37) Weidenthaler, C. Pitfalls in the characterization of nanoporous and nanosized materials. *Nanoscale* **2011**, *3*, 792−810.
(38) Gentile, F. S.; Pannico, M.; Causà, M.; Mensitieri, G.; Di Palma, G.; Scherillo, G.; Musto, P. Metal defects in HKUST-1 MOF revealed by vibrational spectroscopy: A combined quantum mechanical and experimental study. *J. Mater. Chem. A* **2020**, *8*, 10796−10812.
(39) Huo, J.; Brightwell, M.; El Hankari, S.; Garai, A.; Bradshaw, D. A versatile, industrially relevant, aqueous room temperature synthesis of HKUST-1 with high space-time yield. *J. Mater. Chem. A* **2013**, *1*, 15220−15223.
(40) Wang, M.; Hou, T.; Shen, Z.; Zhao, X.; Ji, H. MOF-derived Fe_2O_3: Phase control and effects of phase composition on gas sensing performance. *Sens. Actuators, B* **2019**, *292*, 171−179.
(41) Chen, Y.; Mu, X.; Lester, E.; Wu, T. High efficiency synthesis of HKUST-1 under mild conditions with high BET surface area and CO_2 uptake capacity. *Prog. Nat. Sci.: Mater. Int.* **2018**, *28*, 584−589.
(42) Wang, Y.; Lü, Y.; Zhan, W.; Xie, Z.; Kuang, Q.; Zheng, L. Synthesis of porous Cu_2O/CuO cages using Cu-based metal−organic frameworks as templates and their gas-sensing properties. *J. Mater. Chem. A* **2015**, *3*, 12796−12803.
(43) Al-Janabi, N.; Hill, P.; Torrente-Murciano, L.; Garforth, A.; Gorgojo, P.; Siperstein, F.; Fan, X. Mapping the Cu-BTC metal−organic framework (HKUST-1) stability envelope in the presence of water vapour for CO_2 adsorption from flue gases. *Chem. Eng. J.* **2015**, *281*, 669−677.
(44) Hernández, M. P.; Fernández-Bertrán, J. F.; Farías, M. H.; Díaz, J. A. Reaction of imidazole in gas phase at very low pressure with Cu foil and Cu oxides studied by X-ray photoelectron spectroscopy. *Surf. Interface Anal.* **2007**, *39*, 434−437.
(45) Ahmed, A.; Robertson, C. M.; Steiner, A.; Whittles, T.; Ho, A.; Dhanak, V.; Zhang, H. Cu(I)Cu(II)BTC, a microporous mixed-valence MOF via reduction of HKUST-1. *RSC Adv.* **2016**, *6*, 8902−8905.
(46) Davó-Quiñonero, A.; Bailón-García, E.; López-Rodríguez, S.; Juan-Juan, J.; Lozano-Castelló, D.; García-Melchor, M.; Herrera, F. C.; Pellegrin, E.; Escudero, C.; Bueno-López, A. Insights into the Oxygen Vacancy Filling Mechanism in CuO/CeO_2 Catalysts: A Key Step Toward High Selectivity in Preferential CO Oxidation. *ACS Catal.* **2020**, *10*, 6532−6545.
(47) Gupta, N. K.; Bae, J.; Kim, S.; Kim, K. S. Fabrication of Zn-MOF/ZnO nanocomposites for room temperature H_2S removal: Adsorption, regeneration, and mechanism. *Chemosphere* **2021**, *274*, 129789.
(48) Martin, L.; Martinez, H.; Poinot, D.; Pecquenard, B.; Le Cras, F. Comprehensive X-Ray Photoelectron Spectroscopy Study of the Conversion Reaction Mechanism of CuO in Lithiated Thin Film Electrodes. *J. Phys. Chem. C* **2013**, *117*, 4421−4430.
(49) Gupta, N. K.; Ghaffari, Y.; Kim, S.; Bae, J.; Kim, K. S.; Saifuddin, M. Photocatalytic degradation of organic pollutants over MFe_2O_4 (M = Co, Ni, Cu, Zn) nanoparticles at neutral pH. *Sci. Rep.* **2020**, *10*, 4942.
(50) Travlou, N. A.; Singh, K.; Rodríguez-Castellón, E.; Bandosz, T. J. Cu−BTC MOF−graphene-based hybrid materials as low concentration ammonia sensors. *J. Mater. Chem. A* **2015**, *3*, 11417−11429.
(51) Petit, C.; Mendoza, B.; Bandosz, T. J. Hydrogen Sulfide Adsorption on MOFs and MOF/Graphite Oxide Composites. *ChemPhysChem* **2010**, *11*, 3678−3684.
(52) Kushwah, R.; Singh, A.; Anshul, A.; Mishra, D.; Amritphale, S. S. Facile and controlled synthesis of copper sulfide nanostructures of varying morphology. *J. Mater. Sci.: Mater. Electron.* **2017**, *28*, 5597−5602.
(53) Gupta, A.; Singh, P.; Shivakumara, C. Synthesis of nanoparticles by precipitation method using sodium hexa metaphosphate as a stabilizer. *Solid State Commun.* **2010**, *150*, 386−388.
(54) Sifontes, Á. B.; Cañizales, E.; Toro-Mendoza, J.; Ávila, E.; Hernández, P.; Delgado, B. A.; Gutiérrez, G. B.; Díaz, Y.; Cruz-Barrios, E. Obtaining Highly Crystalline Barium Sulphate Nanoparticles via Chemical Precipitation and Quenching in Absence of Polymer Stabilizers. *J. Nanomater.* **2015**, *2015*, 1−8.
(55) Petit, C.; Bandosz, T. J. Exploring the coordination chemistry of MOF−graphite oxide composites and their applications as adsorbents. *Dalton Trans.* **2012**, *41*, 4027−4035.
(56) Rani, B. J.; Ravi, G.; Yuvakkumar, R.; Velauthapillai, D.; Saravanakumar, B.; Al-Mohaimeed, A. M. Investigation on copper based oxide, sulfide and selenide derivatives oxygen evolution reaction activity. *Appl. Nanosci.* **2020**, *10*, 4299−4306.
(57) Nyquist, R. Thiols, sulfides and disulfides, alkanethiols, and alkanedithiols (S-H stretching). In *Interpreting Infrared, Raman, and Nuclear Magnetic Resonance Spectra*; Vol. 2; Elsevier, 2001; pp. 65−83.
(58) Jin, M.; Qian, X.; Gao, J.; Chen, J.; Hensley, D. K.; Ho, H. C.; Percoco, R. J.; Ritzi, C. M.; Yue, Y. Solvent-Free Synthesis of CuO/HKUST-1 Composite and Its Photocatalytic Application. *Inorg. Chem.* **2019**, *58*, 8332−8338.
(59) Nazim, M.; Khan, A. A. P.; Asiri, A. M.; Kim, J. H. Exploring Rapid Photocatalytic Degradation of Organic Pollutants with Porous CuO Nanosheets: Synthesis, Dye Removal, and Kinetic Studies at Room Temperature. *ACS Omega* **2021**, *6*, 2601−2612.
(60) Ayodhya, D.; Venkatesham, M.; Santoshi Kumari, A.; Reddy, G. B.; Ramakrishna, D.; Veerabhadram, G. Photocatalytic degradation of dye pollutants under solar, visible and UV lights using green synthesised CuS nanoparticles. *J. Exp. Nanosci.* **2016**, *11*, 418−432.
(61) Pal, M.; Mathews, N. R.; Sanchez-Mora, E.; Pal, U.; Paraguay-Delgado, F.; Mathew, X. Synthesis of CuS nanoparticles by a wet chemical route and their photocatalytic activity. *J. Nanopart. Res.* **2015**, *17*, 301.
(62) Kao, Y.-T.; Yang, S.-M.; Lu, K.-C. Synthesis and Photocatalytic Properties of CuO-CuS Core-Shell Nanowires. *Materials* **2019**, *12*, 1106.
(63) Pillai, V. V.; Lonkar, S. P.; Alhassan, S. M. Template-Free, Solid-State Synthesis of Hierarchically Macroporous S-Doped TiO_2 Nano-Photocatalysts for Efficient Water Remediation. *ACS Omega* **2020**, *5*, 7969−7978.
(64) Devi, L. G.; Kavitha, R. Enhanced photocatalytic activity of sulfur doped TiO_2 for the decomposition of phenol: A new insight into the bulk and surface modification. *Mater. Chem. Phys.* **2014**, *143*, 1300−1308.

https://doi.org/10.1021/acsomega.1c03712
ACS Omega 2021, 6, 25631−25641